
DynPoint: Dynamic Neural Point For View Synthesis

Kaichen Zhou, Jia-Xing Zhong, Sangyun Shin, Kai Lu,
Yiyuan Yang, Andrew Markham, Niki Trigoni

Department of Computer Science
University of Oxford

{rui.zhou, jiaxing.zhong, sangyun.shin, kai.lu}@cs.ox.ac.uk
{yiyuan.yang, andrew.markham, niki.trigoni}@cs.ox.ac.uk

Abstract

The introduction of neural radiance fields has greatly improved the effectiveness of view synthesis for monocular videos. However, existing algorithms face difficulties when dealing with uncontrolled or lengthy scenarios, and require extensive training time specific to each new scenario. To tackle these limitations, we propose DynPoint, an algorithm designed to facilitate the rapid synthesis of novel views for unconstrained monocular videos. Rather than encoding the entirety of the scenario information into a latent representation, DynPoint concentrates on predicting the explicit 3D correspondence between neighboring frames to realize information aggregation. Specifically, this correspondence prediction is achieved through the estimation of consistent depth and scene flow information across frames. Subsequently, the acquired correspondence is utilized to aggregate information from multiple reference frames to a target frame, by constructing hierarchical neural point clouds. The resulting framework enables swift and accurate view synthesis for desired views of target frames. The experimental results obtained demonstrate the considerable acceleration of training time achieved - typically an order of magnitude - by our proposed method while yielding comparable outcomes compared to prior approaches. Furthermore, our method exhibits strong robustness in handling long-duration videos without learning a canonical representation of video content. More details can be found at <https://github.com/kaichen-z/DynPoint>.

1 Introduction

The computer vision community has directed significant attention towards novel view synthesis (VS) due to its potential for both emerging techniques in artificial reality and also to enhance a machine's ability to comprehend the appearance and geometric properties of target scenarios [36, 8, 38]. State-of-the-art techniques leveraging neural rendering algorithms, as demonstrated in studies such as [36, 59, 62], have successfully attained photorealistic reconstruction of views in static scenarios. However, the dynamic characteristics inherent to most real-world scenarios present a formidable challenge to the suitability of existing approaches that rely on the epipolar geometric relationship, traditionally applicable to static scenarios [23, 45].

Recent studies have primarily focused on the synthesis of views in dynamic scenarios by employing one or multiple multilayer perceptrons (MLPs) to encode the essential spatiotemporal information of the scene [45, 30, 42, 41]. In one approach, a latent representation is generated to encompass the comprehensive per-frame details of the target video [30, 17, 63]. Although this method is capable of producing visually realistic results, its applicability is limited to short videos due to the constrained memory capacity of MLPs or other representation mechanisms [31]. Alternatively, another approach seeks to construct a latent representation of canonical scenarios and establish correspondences between individual frames and the canonical scenario [45, 42, 64]. This alternative approach allows for the processing of long-term videos; however, it imposes specific requirements on the video

characteristics being learned. For instance, the videos should consistently feature similar objects across frames, and some algorithms may require prior knowledge about the video [61, 43].

In order to address this challenge, we introduce DynPoint, a novel approach designed to achieve efficient view synthesis of lengthy monocular videos without the need for learning a latent canonical representation. Unlike conventional methods that encode information implicitly, DynPoint employs an explicit estimation of consistent depth and scene flow for surface points. These estimates are subsequently utilized to aggregate information from reference frames into the target frame. Subsequently, hierarchical neural point clouds are constructed based on the aggregated information. This hierarchical point cloud set is then employed to synthesize views of the target frame. Our contributions can be summarized as follows:

- We introduce a novel module to estimate consistent depth information for monocular video with the help of a proposed regularization and training strategy.
- We propose an efficient approach to estimate smooth scene flow between adjacent frames with the proposed training strategy by leveraging the estimated consistent depth maps.
- We present a representation to aggregate information from reference frames to target frame, facilitating rapid view synthesis of the target frame within a monocular video.
- Comprehensive experiments are conducted on datasets including Nerfie, Nvidia, HyperNeRF, Iphone, and Davis showcasing the speed and accuracy of DynPoint for view synthesis.

2 Related Works

2.1 Static View Synthesis

The generation of photo-realistic views from arbitrary input viewing angles has been a longstanding challenge in the field of computer vision. In the scenario of static scenes, early approaches addressed the challenge of synthesizing photo-realistic views by employing local warping techniques to handle densely sampled views [20, 29, 2, 5, 7]. Additionally, the gradient domain was utilized to handle the single-view case [28]. In order to tackle the challenges associated with view synthesis, several subsequent works have been developed. These works aim to address issues such as reflections, repetitive patterns, and untextured regions [27, 16, 25, 15, 48, 10, 33, 35, 40, 51, 52, 53, 54, 60, 73]. In more recent developments, researchers have explored the representation of scenes as continuous neural radiance fields (NeRF) using fully connected neural networks. These works, such as [37, 1, 67], have demonstrated remarkable outcomes with a trade-off between accuracy and computational complexity (i.e., one network for one scene). To tackle the computational burden associated with neural radiance fields, recent works have focused on developing approaches that generalize the representation across multiple scenes using a single network. These methods employ various techniques, such as fully-convolutional architectures [66], plane-swept cost volumes [8], image-based rendering [59], disentanglement of shape and texture [72], utilization of local features in 2D [57], as well as generative methods [6, 50, 39, 21, 3].

2.2 Dynamic View Synthesis

The emergence of static scene advancements has spurred interest in the exploration of view synthesis for dynamic scenes within the field. Previous research efforts have expanded upon studies conducted in static scenes, incorporating elements such as globally coherent depth [65] and 3D mask volume [32]. Recent research direction builds upon the concept of NeRF and extends it to dynamic scenes by integrating time into the learning process of spatio-temporal radiance fields. One category of research focuses on the assumption of a canonical scenario that spans the entire video [4, 11, 22]. Deformable radiance field-based approaches, as described in previous works [45, 56, 41, 14, 34], employ temporal warping techniques to adapt a base NeRF representation of the canonical space for dynamic scenes. This enables the synthesis of novel views in the context of long monocular videos. Another category of algorithms aims to encode the temporal dynamics of the scene into a global representation. [30] employs a MLP to model the 3D dense motion, resulting in a spatial-temporal NeRF. Building upon this, [13, 58, 17] demonstrate that introducing additional regularization techniques that encourage consistency and physically plausible solutions can enhance the accuracy of view reconstruction. The first category of methods, while achieving impressive photorealistic results, is constrained by the requirement for object-centric videos, thus limiting their generalizability to diverse scenarios.

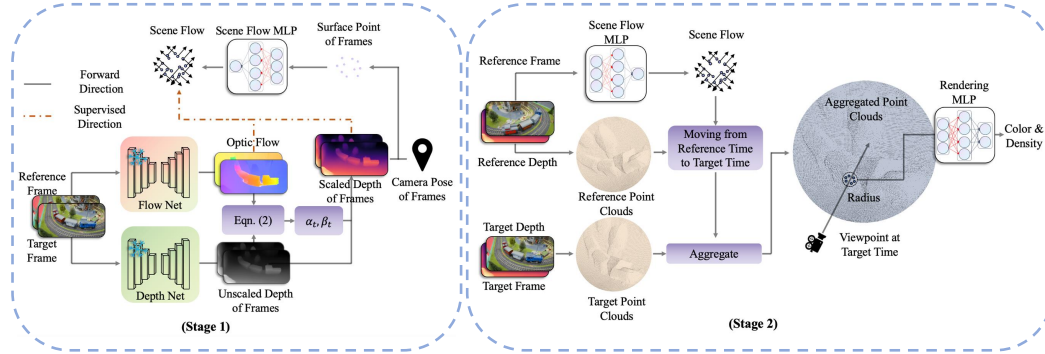


Figure 1: **Structure of DynPoint.** The **Stage 1** shows the pipeline of consistent depth estimation in Sec. 3.2 and scene flow estimation in Sec. 3.3. Initially, the frames are employed in the Flow Net, Depth Net, and Scale Parameters to produce optic flows and depth. Then, surface points are calculated based on the estimated depth and utilized in the Scene Flow MLP. The **Stage 2** shows the process of information aggregation presented in Sec. 3.4. Neural Point Clouds is firstly generated based on pre-computed scene flow. The Rendering MLP utilizes all neural points located within a specified radius from the queried point as inputs to predict the final color and density.

Conversely, the second category of methods encounters difficulties when dealing with long videos, leading to limitations in effectively handling such scenarios. To address the aforementioned issue, our algorithm focuses on achieving novel synthesis by aggregating information from the reference frame to the target frame. This information aggregation process is accomplished by explicitly modeling the object movement and depth information. As a result, our algorithm exhibits significant advancements in both accuracy and speed.

3 Methodology

3.1 Overview

Our algorithm is designed to realize view synthesis for a dynamic scenario by utilizing a monocular video $\{I_1, I_2, \dots, I_T\}$. The frames in the video, denoted by I_t , are captured by a known camera $C_{t,c} = \{K_{t,c} | [R_{t,c}, t_{t,c}]\}$, where c denotes known camera viewpoint. The objective is to generate the novel view from a specified viewpoint q at a desired time frame $C_{t,q} = \{K_{t,q} | [R_{t,q}, t_{t,q}]\}$.

Consistent with previous researches [30, 17, 18, 31, 34, 63], we adopt a training paradigm in which our model is trained on the input monocular video with the assistance of pre-trained optic flow and monocular depth models [47, 55, 26]. During the training process, the RGB information obtained from the observed viewpoint is utilized as the supervision signal, without relying on any canonical information. Subsequently, the trained model is evaluated on the task of synthesizing corresponding RGB, depth and scene flow information for unobserved viewpoints.

In contrast to previous methods that utilize one or multiple MLPs to encode the 3D information of each frame, our work focuses on establishing correspondence relationships, i.e., scene flow, between the 3D surface points of the current frame and those of adjacent frames. We can infer 3D information about unobserved points of the current frame by aggregating the information from adjacent frames.

To realize the aforementioned concept, our proposed model should undertake three key tasks. The first task is to estimate depth information consistently for each frame, as outlined in Sec. 3.2. The second task involves learning the 3D scene flow between the current frame and its adjacent frames, as detailed in Sec. 3.3. These two processes are demonstrated in the stage 1 of Fig. 1. The final task is to aggregate information based on learned correspondence and subsequently use this information to realize view synthesis, as discussed in Sec. 3.4. This process is shown in the stage 2 of Fig. 1.

3.2 Consistent Depth Estimation

Despite the ability of current monocular depth methods [47, 46] to produce accurate depth priors, the predicted depth maps D'_t suffer from scale-variance and shift problems when compared to the

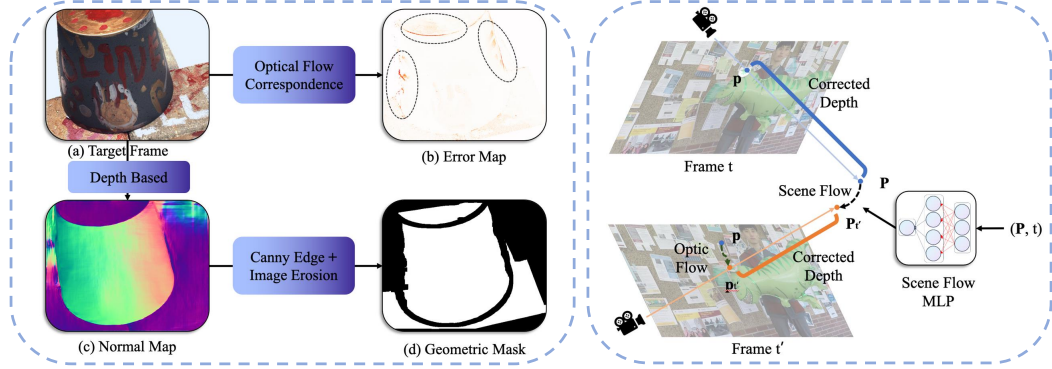


Figure 2: **Demonstration of Geometric Edge Mask and Scene Flow Estimation.** The **left** section depicts the conceptual basis for designing the Geometric Edge Mask. The **right** part demonstrates the construction of the scene flow objective function shown in Sec. 3.3.

ground truth depth [19, 71, 69]. This characteristic renders D'_t inconsistent across the temporal axis of monocular video. Moreover, since the optic flow $f_{t \rightarrow t'}$ between frames could be predicted from a pretrained model, a depth value \bar{D}_t can be computed using the triangulation relation between frames, along with the camera parameters and Mid-point method. Compared to D'_t , \bar{D}_t can have consistent scaling across frames. However, \bar{D}_t heavily relies on $f_{t \rightarrow t'}$ and Epipolar constraint, and it can only generate accurate depth information for a limited portion of the frame. The first module of DynPoint aims to combine D'_t and \bar{D}_t to generate the final consistent depth estimation \hat{D}_t .

Regularization: To address this issue, DynPoint identifies the accurate region of \bar{D}_t by utilizing three masks: the corresponding mask, the geometric edge mask, and the dynamic object mask.

Correspondence Mask $\mathcal{M}_{c,t \rightarrow t'}$: The purpose of the optic flow is to capture the pixel-wise correspondence between two frames, making it accurate only for the corresponding regions. These regions can be identified by masking out areas of occlusion caused by both ego-motion and object movement. This Correspondence Mask could be formulated as follow:

$$\mathcal{M}_{c,t \rightarrow t'} = \begin{cases} 0 & \text{if } |f_{t \rightarrow t'}(\mathbf{p}) + f_{t' \rightarrow t}(\mathbf{p} + f_{t \rightarrow t'}(\mathbf{p}))| > \epsilon_c, \\ 1 & \text{if } |f_{t \rightarrow t'}(\mathbf{p}) + f_{t' \rightarrow t}(\mathbf{p} + f_{t \rightarrow t'}(\mathbf{p}))| \leq \epsilon_c, \end{cases} \quad (1)$$

where ϵ_c is a predefined threshold for the correspondence mask.

Geometric Edge Mask \mathcal{M}_g : Furthermore, it has been observed that the reliability of \bar{D}_t diminishes when applied to geometric edges as in Fig. 2, particularly in areas where the optic flow exhibits non-smooth characteristics. To compute the mask \mathcal{M}_g , we first estimate the normal vector map of the surface $\mathbf{n} = (-\frac{dz}{dx}, -\frac{dz}{dy}, 1) / \|(-\frac{dz}{dx}, -\frac{dz}{dy}, 1)\|$ with the help of \bar{D}_t . Then we apply the Canny edge detector [12] on the $\mathbf{n} \in \mathbb{R}^{H \times W \times 3}$ to generate the estimation of geometric edge. The intuition of the geometric edge mask is demonstrated in the left part of Fig. 2. From the error map shown in Fig. 2(b), it is evident that the errors primarily manifest around the geometric boundaries of the scenario.

Dynamic Object Mask \mathcal{M}_d : In addition to the two masks mentioned above, a Dynamic Object Mask is necessary to exclude the dynamic regions of the frame where the triangulation relationship does not hold. Similar to [17], we combine the MASK R-CNN [24] with the Sampson error to generate the \mathcal{M}_d . In order to obtain a valid mask with high accuracy, we apply *image erosion* to \mathcal{M}_d , \mathcal{M}_c and \mathcal{M}_g to mitigate inaccurate boundary detection.

Objective Function: Based on the above three masks, the reliable region of the \bar{D}_t could be masked out by using the final mask $\mathcal{M}_f = \mathcal{M}_c \cap \mathcal{M}_g \cap \mathcal{M}_d$. To combine the information of D'_t and \bar{D}_t , we assume that the consistent depth map $\hat{D}_t \in \mathbb{R}^{H \times W}$ could be approximated by using D'_t , a scale variable $\alpha_t \in \mathbb{R}$ and a shift variable $\beta_t \in \mathbb{R}$. The parameters α_t and β_t can be generated by optimizing:

$$\alpha_t, \beta_t = \operatorname{argmin} \mathcal{M}_f \odot |\bar{D}_t - (\alpha_t D'_t + \beta_t)|. \quad (2)$$

Training Strategy: Dependent solely on the nearest frame for the computation of \overline{D}_t would lack sufficient reliability due to the combined influence of the accuracy of the camera matrix and the accuracy of the optic flow on the triangulation process. We employ a series of adjacent $2K$ frames to calculate the triangulated depth set denoted as $\{\overline{D}_t^k\}_{k=1}^{2K}$. Instead of directly utilizing all $\{\overline{D}_t^k\}_{k=1}^{2K}$ in Eqn. 2, we perform a reevaluation by recomputing the intersection mask as $\mathcal{M}_f = \mathcal{M}_f^1 \cap \dots \cap \mathcal{M}_f^{2K}$, which further refines the triangulated depth \overline{D}_t , ensuring the appropriate scale constraint for D'_t . It's worth noting that pose estimation may not be accurate for dynamic scenarios in certain datasets, as it relies on COLMAP-based estimation. In such cases, we utilize the algorithm presented in our Supplementary material to enhance and fine-tune the pose estimation.

3.3 Scene Flow Estimation

Combined with estimated consistent depth map \hat{D}_t and optic flow $f_{t \rightarrow t'}$, DynPoint also aims to infer the scene flow $s_{t \rightarrow t'}$ to build the 3D correspondence between the current frame and adjacent frames. Unlike previous works [41, 45, 56, 14], which estimate the trajectory of all points (hundreds of sampled points on the ray of each point) in the scenario, DynPoint only infers the trajectory of surface point (one point on the ray of each point) of the frame to accelerate both training and inference process. To realize this process, we use a MLP to estimate the scene flow, which can be written as $\Delta P_{t \rightarrow t+1}, \Delta P_{t \rightarrow t-1} = F_\theta(P, t)$ where $P \in \mathcal{R}^3$ denotes input 3D point; $\Delta P_{t \rightarrow t'}$ denotes the trajectory of P from t to t' . The weight θ can be optimized by using the relationship among the depth \hat{D}_t , the optic flow $f_{t \rightarrow t'}$ and the scene flow $s_{t \rightarrow t'}$.

Objective Function: Given a pixel p_t in frame t , its corresponding pixel in frame t' , denoted as $p_{t'}$, can be obtained by adding the 2D flow $f_{t \rightarrow t'}(p_t)$ to p_t . Additionally, utilizing the depth map \hat{d}_t and camera matrix C_t , which are available at frame t , the 3D point corresponding to p_t can be expressed as $P_t = R_t K_t^{-1} \hat{D}_t(p_t) p_t + t_t$. The same method can be used to compute $P_{t'}$. Thus, we've:

$$s_{t \rightarrow t'}(p_t) = \hat{D}_{t'}(p_t + f_{t \rightarrow t'}(p_t)) R_{t'} K_{t'}^{-1} (p_t + f_{t \rightarrow t'}(p_t)) + t_{t'} - P_t. \quad (3)$$

This process is demonstrated in the right part of Fig. 2. For static part masked by \mathcal{M}_d , we set $s_t(p_t) = 0$. For the dynamic part, the loss function can be written as

$$\mathcal{L}_s = \sum_{p_t \in \mathcal{M}_c \cap \mathcal{M}_g \cap \neg \mathcal{M}_d} |s_{t \rightarrow t'}(p_t) - \Delta P_{t \rightarrow t'}|. \quad (4)$$

In order to enhance the accuracy of scene flow estimation for the dynamic elements within the scenario, we employ the cycle constraint, a well-established technique utilized in prior studies [17, 34]. The cycle constraint can be expressed as follows:

$$\mathcal{L}_c = \sum_{p_t \in \neg \mathcal{M}_d} |\Delta P_{t \rightarrow t+k} + \Delta P_{t+k \rightarrow t}(P_t + \Delta P_{t \rightarrow t+k})|. \quad (5)$$

Training Strategy: We have observed that optimizing Eqn. 4 solely with the near frames, where $t' = t - 1$ or $t + 1$, does not produce accurate results for further information aggregation. To reconstruct the 3D information of the current frame, it is necessary to compute the correspondence between the current frame and $2K$ adjacent frames, in order to aggregate sufficient information. During the training process, we compute the scene flow between frame t and its $2K$ adjacent frames, where $K \in \{1, \dots, K\}$. We then utilize Eqn. 4 to form the loss function between current frame and $2K$ adjacent frames. The scene flow $\Delta P_{t \rightarrow t+k}$ could be written as:

$$\Delta P_{t \rightarrow t+k} = F_\theta(P_t, t)[0] + \dots + F_\theta(P_t + \Delta P_{t \rightarrow t+k-1}, t+k-1)[0]. \quad (6)$$

It's important to mention that achieving better results can be accomplished by fine-tuning the refinement layers of the pre-trained depth network.

3.4 View Synthesis

Information Aggregation: In order to collate data from the $2K$ reference frames to the target frame t , the pixels in the reference frame p_{t+k} are transformed into 3D space as P_{t+k} through the utilization

Table 1: **Novel View Synthesis Results on Nvidia Dataset.** We report the average PSNR and LPIPS results with comparisons to existing methods on Nvidia dataset [65]. * denotes the number adopted from DynamicNeRF [17]. The best performance is **highlighted**. The second-best is also **emphasized**.

PSNR \uparrow / LPIPS \downarrow	Jumping	Skating	Truck	Umbrella	Balloon1	Balloon2	Playground	Average
NeRF* [37] (~ 24 hours)	20.99 / 0.305	23.67 / 0.311	22.73 / 0.229	21.29 / 0.440	19.82 / 0.205	24.37 / 0.098	21.07 / 0.165	21.99 / 0.250
NeRF + time*[37](~ 24 hours)	18.04 / 0.455	20.32 / 0.512	18.33 / 0.382	17.69 / 0.728	18.54 / 0.275	20.69 / 0.216	14.68 / 0.421	18.33 / 0.427
D-NeRF [45] (> 20 hours)	22.36 / 0.193	22.48 / 0.323	24.10 / 0.145	21.47 / 0.264	19.06 / 0.259	20.76 / 0.277	20.18 / 0.164	21.48 / 0.232
NSFF* [30](~ 24 hours)	24.65 / 0.151	29.29 / 0.129	25.96 / 0.167	22.97 / 0.295	21.96 / 0.215	24.27 / 0.222	21.22 / 0.212	24.33 / 0.199
DynamicNeRF* [17] (> 36 hours)	24.68 / 0.090	32.66 / 0.035	28.56 / 0.082	23.26 / 0.137	22.36 / 0.104	27.06 / 0.049	24.15 / 0.080	26.10 / 0.082
HyperNeRF [42] (> 24 hours)	18.34 / 0.302	21.97 / 0.183	20.61 / 0.205	18.59 / 0.443	13.96 / 0.530	16.57 / 0.411	13.17 / 0.495	17.60 / 0.367
TiNeuVox [14] (~ 45 mins)	20.81 / 0.247	23.32 / 0.152	23.86 / 0.173	20.00 / 0.355	17.30 / 0.353	19.06 / 0.279	13.84 / 0.437	19.74 / 0.285
RoDYN [34] (> 36 hours)	25.66 / 0.071	28.68 / 0.040	29.13 / 0.063	24.26 / 0.089	22.37 / 0.103	26.19 / 0.054	24.96 / 0.048	25.89 / 0.065
DynPoint (~ 30 mins)	24.69 / 0.097	31.34 / 0.045	29.30 / 0.061	24.59 / 0.086	22.77 / 0.099	27.63 / 0.049	25.37 / 0.039	26.53 / 0.068

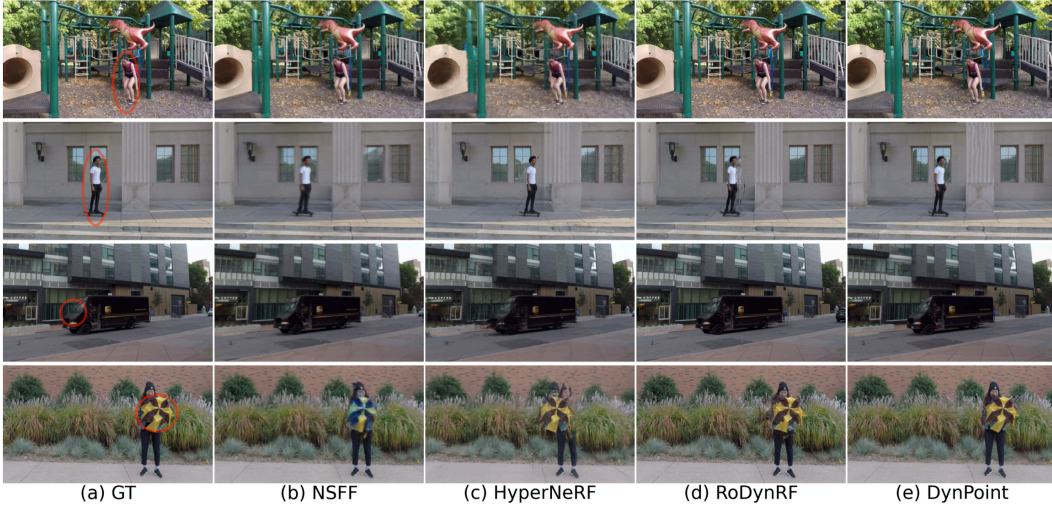


Figure 3: **Demonstration of View Synthesis Results on Nvidia Dataset.** This demonstration compares the view synthesis outcomes of DynPoint with those of NSFF, HyperNeRF, and RoDynRF.

of the corresponding depth value \hat{D}_{t+k} and the matrix C_{t+k} . Next, the DynPoint evaluates the scene flow $\Delta P_{t+k \rightarrow t}$ between frame t and frame $t+k$ by implementing Eqn. 6. By utilizing both the scene flow $\Delta P_{t+k \rightarrow t}$ and the 3D point P_{t+k} , we are able to calculate the 3D point $P_{t+k \rightarrow t}$ that corresponds to reference frame $t+k$ at the target frame t . This is achieved by applying the following computation: $P_{t+k \rightarrow t} = P_{t+k} + \Delta P_{t+k \rightarrow t}$. Additionally, a pre-trained 2D convolutional neural network (CNN) is utilized to generate a 2D image feature vector \mathcal{F} , which is subsequently allocated to each of the points corresponding to pixels.

Finally, we propose the introduction of a hierarchical neural point cloud construction approach to enhance the "perception field" of individual points. This technique aims to address the problem of surface irregularities that may arise from using current monocular depth estimation methods in multi-view depth map fusion. Thus, the point cloud of current frame t could be generated by combining $2K+1$ point clouds as follows:

$$\hat{P}_t = \left\{ \sum_{k=-K}^K P_{t+k \rightarrow t}^h, P_t^h, \sum_{k=-K}^K \mathcal{F}(P_{t+k \rightarrow t}^h), \mathcal{F}(P_t^h) \right\}_{h=1}^H, \quad (7)$$

where H is the number of hierarchical levels. In our case, we set $H=3$. At each step within this framework, we perform a downsampling operation on the neural point cloud (the downsampling procedure is implemented within the point cloud generation process, whereby the depth map and scene map are downsampled using linear interpolation technique; it is important to note that when downsampling the depth map, the intrinsic matrix should also be adjusted accordingly to maintain accurate spatial information.), reducing its resolution by a factor of 2.

View Synthesis: Given a 3D position q and view direction d , we leverage M proximate neural points within a radius of R to generate the corresponding density and color data δ, c as in [62]. This process is shown in the right part of Fig. 1. This can be expressed as follows:

$$(\delta, c) = F_\phi(q, d, \hat{P}_t^1, \mathcal{F}_t^1(\hat{P}_t^1), \gamma_t^1, \dots, \hat{P}_t^M, \mathcal{F}_t^M(\hat{P}_t^M), \gamma_t^M). \quad (8)$$

Table 2: **Novel View Synthesis Results on Nerfie Dataset.** We report the average PSNR and LPIPS results with comparisons to existing methods on Nerfie dataset [41].

PSNR \uparrow / LPIPS \downarrow	CURLS	TOBY SIT	TAIL	BROOM	Average
NeRF [37]	14.40 / 0.616	22.80 / 0.463	23.00 / 0.571	21.00 / 0.667	20.30 / 0.579
NeRF + time[37]	17.30 / 0.539	19.40 / 0.385	24.90 / 0.404	21.90 / 0.576	20.87 / 0.476
NSFF [30]	18.00 / 0.432	26.90 / 0.208	30.60 / 0.245	28.20 / 0.202	<u>25.93</u> / 0.272
Nerfies [41]	24.90 / 0.312	22.80 / 0.174	23.60 / 0.175	21.00 / 0.270	23.08 / 0.233
DynPoint	<u>24.33</u> / <u>0.339</u>	<u>24.90</u> / <u>0.186</u>	<u>29.12</u> / <u>0.218</u>	<u>27.28</u> / <u>0.222</u>	26.41 / <u>0.241</u>



Figure 4: **Demonstration of View Synthesis Results on Nerfie Dataset.** This demonstration compares the view synthesis outcomes of DynPoint with those of NSFF.

where γ_t^1 is the per-point confidence introduced in [62]. Finally, we make use the rendering process in [37] to predict final RGB value C as:

$$C = \sum_{j=1}^N \tau_j (1 - \exp(-\sigma_j \delta_j)) c_j, \quad (9)$$

where $\tau_j = \exp(-\sum_{t=1}^{j-1} \sigma_t \delta_t)$; δ_j denotes the distance between adjacent shading samples; c_j is the color information and δ_j is the density information. The L2 loss function is used to supervise our rendered pixel values similar to the setting of [36]. For further information regarding the network architecture, please consult our supplementary materials.

3.5 Discussion

The purpose of this section is to explicate the dissimilarities between the DynPoint and a recently published concurrent work, namely DynIBaR [31] which was released in March 2023 and currently lacks available code. Both DynIBaR and DynPoint harness information aggregation mechanisms to realize the synthesis of novel views. However, DynIBaR predominantly centers around the aggregation of information through two-dimensional (2D) pixel units. This approach draws inspiration from image-based rendering principles, entailing the synthesis of novel perspectives from a collection of reference images via a weighted fusion of reference pixels. In contrast, DynPoint’s focal point lies in the information aggregation achieved by constructing three-dimensional (3D) neural point clouds. The final novel view synthesis is realized by using neural points surrounding queries’ position.

Moreover, DynPoint introduces an efficacious strategy for the seamless integration of monocular depth estimation within the ambit of monocular video view synthesis. In contrast to DynIBaR, which endeavors to model the trajectory of all samples (128) traversing each ray, DynPoint exclusively focuses on the trajectory of surface points, thereby yielding a substantial acceleration in both training and inference stage.

Table 3: **Novel View Synthesis Results of HyperNeRF Dataset.** We report the average PSNR and LPIPS results with comparisons to existing methods on HyperNeRF dataset [42].

PSNR \uparrow / LPIPS \downarrow	Broom 197 Frames	3D printer 207 Frames	Chicken 164 Frames	Expressions 259 Frames	Peel Banana 513 Frames	Average
NSFF [30]	26.10 / 0.284	27.70 / 0.125	26.90 / 0.106	26.70 / 0.157	24.60 / 0.198	26.40 / 0.174
Nerfies [41]	19.20 / 0.325	20.60 / 0.108	26.70 / 0.078	21.80 / 0.150	22.40 / 0.147	22.10 / 0.162
Hyper-NeRF [42]	20.60 / 0.613	21.40 / 0.212	27.60 / 0.108	22.00 / 0.196	24.30 / 0.170	23.20 / 0.260
DynPoint	27.40 / 0.248	27.60 / 0.163	28.10 / 0.089	27.90 / 0.147	26.50 / 0.129	27.50 / 0.155

Table 4: **Novel View Synthesis Results of Iphone Dataset.** We compare the mPSNR and mSSIM scores with existing methods on the iPhone dataset [18].

mPSNR \uparrow / mSSIM \uparrow	Apple	Block	Paper-windmill	Space-out	Spin	Teddy	Wheel	Average
NSFF [30]	17.54 / 0.750	16.61 / 0.639	17.34 / 0.378	17.79 / 0.622	18.38 / 0.585	13.65 / 0.557	13.82 / 0.458	15.46 / 0.569
Nerfies [41]	17.64 / 0.743	17.54 / 0.670	17.38 / 0.382	17.93 / 0.605	19.20 / 0.561	13.97 / 0.568	13.99 / 0.455	16.45 / 0.569
HyperNeRF [42]	16.47 / 0.754	14.71 / 0.606	14.94 / 0.272	17.65 / 0.636	17.26 / 0.540	12.59 / 0.537	14.59 / 0.511	16.81 / 0.550
DynPoint	17.78 / 0.743	17.67 / 0.667	17.32 / 0.366	17.78 / 0.603	19.04 / 0.564	13.95 / 0.551	14.72 / 0.515	16.89 / 0.572

4 Experiment

4.1 Experimental Setting

To evaluate the view synthesis capabilities of DynPoint, we performed experiments on four extensively utilized datasets, namely Nvidia dataset in [30], Nerfie in [41], HyperNeRF in [42] and Iphone in [18]. It is noteworthy to mention that the official website of Nerfie [41] only provides four specific scenarios. Consequently, our experiments were solely conducted on provided four scenarios as in [18]. Additionally, we also assessed DynPoint’s performance on a recent dataset Iphone [18], which specifically addresses the challenge of camera teleportation. Furthermore, we examined the efficacy of monocular depth estimation and scene estimation by visualizing the results obtained from the Davis dataset, as in [68].

We conducted a comparative analysis of our work with several recent methods, based on the reported results in their original papers or the reimplementations of their official code. The methods we compared with include NeRF [37], NeRF + time [37] (which directly utilizes embedded time information as an input to encode all information of the target dynamic scenario), D-NeRF [45], NSFF [30], DynamicNeRF [17], HyperNeRF [42], Nerfie [41], TiBeuVox [14], and RoDYN [34]. In our research, we employed the pretrained Deep Pruning Transformer (DPT) network in [46], for monocular depth estimation. For optic flow estimation, we utilized the pretrained FlowFormer model [26]. To facilitate the fine-tuning process, we initialized the weights of the Rendering MLP by pretraining it on the DTU dataset, employing a similar training set to that used in [62].

The per-scenario training time is shown in Tab. 1. A notable observation was made regarding the reduced per-scenario training time of DynPoint in comparison to other algorithms. This enhancement can be attributed to the implementation of a two-step strategy. In the initial stage, the optimization process focuses on a limited set of parameters pertaining to monocular depth estimation and scene flow estimation. Subsequently, for the second stage, leveraging the outcomes obtained from the first stage, the generation of the neural point cloud for subsequent view synthesis is achieved successfully. Furthermore, the pretraining stage also contributes to the efficiency of our view synthesis stage, requiring only a few iterations to produce desirable results on novel scenarios.

Nvidia (Tab. 1): During this experiment, it was observed that DynPoint exhibited superior performance compared to other algorithms in terms of peak signal-to-noise ratio (PSNR). Additionally, DynPoint achieved the second highest ranking among all algorithms when evaluated based on the Learned Perceptual Image Patch Similarity (LPIPS) metric. Even for scenarios involving multiple objectives, such as Jumping, DynPoint demonstrates reasonable performance without requiring the learning of any canonical representation or extensive training time. The results of specific partial scenarios, namely Playground, Skating, Truck, and Umbrella, are presented in Fig. 3. Notably, leveraging monocular depth estimation, DynPoint generally produces views with improved geometric features, as evident in the Skating case shown in the second row of Fig. 3. Even in challenging scenarios like Umbrella, DynPoint successfully generates high-quality views while minimizing blurring effects. **Nerfie** (Tab. 2): In the case of the extended scenario, DynPoint exhibits superior performance in terms of PSNR and achieves comparable results to those obtained in the short video Nvidia, as presented in Tab. 2. This achievement can be attributed to our information aggregation

Table 5: **Ablation studies of Nvidia Dataset.** We report the average PSNR and LPIPS results with comparisons to existing methods on Nvidia dataset [65].

PSNR \uparrow / LPIPS \downarrow	Jumping	Skating	Truck	Umbrella	Balloon1	Balloon2	Playground	Average
w/o multiple-step strategies	15.01 / 0.711	17.43 / 0.691	15.36 / 0.606	14.90 / 0.837	13.98 / 0.583	15.46 / 0.624	11.35 / 0.613	14.78 / 0.666
w/ $K = 3$	20.22 / 0.262	22.53 / 0.274	22.38 / 0.291	19.13 / 0.383	16.59 / 0.413	16.92 / 0.459	14.83 / 0.416	18.94 / 0.357
w/o Hierarchical Point Cloud	23.82 / 0.174	28.74 / 0.053	27.50 / 0.085	22.73 / 0.192	21.08 / 0.256	24.67 / 0.180	22.14 / 0.189	24.38 / 0.161
DynPoint ($K = 6$)	24.69 / 0.097	31.34 / 0.045	29.30 / 0.061	24.59 / 0.086	22.77 / 0.099	27.63 / 0.049	25.37 / 0.039	26.53 / 0.068

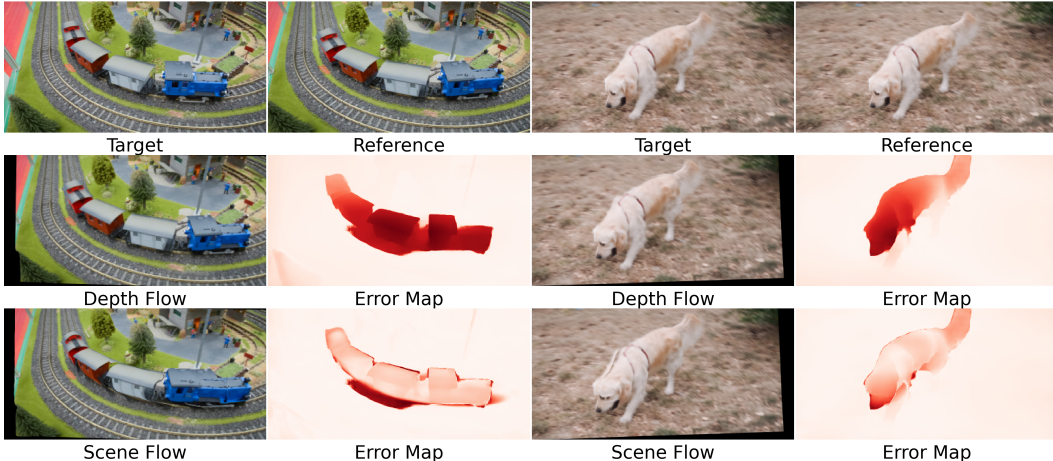


Figure 5: **Demonstration of Depth and Scene Flow Estimation.** This figure presents the output of the target images obtained by warping the reference image using depth estimation (second row) or using both depth and scene flow estimation (third row). It is important to clarify that the figure is **not intended for comparing view synthesis results**. The synthesized figures generated based on scene flow inherently incorporate object motion as input, resulting in observable **motion blur** within the synthesized figures. Additionally, an error map represented by the intensity of red is provided to visualize the performance, where deeper shades of red indicate larger errors (in terms of pixel movement compared to corrected optic flow).

approach, which focuses on effectively aggregating information from the target frame by establishing associations between its points and those in the reference frames. Novel view synthesis results for scenarios TAIL and TOBY SIT are depicted in Figure 4. It is evident that for longer videos, DynPoint continues to produce more realistic frames. Notably, the generated views in this figure do not exist in either the training or test dataset. **HyperNeRF** (Tab. 3): In the case of longer video sequences, DynPoint showcases superior performance in PSNR, as highlighted in Table 3. **iPhone** (Tab. 4): In the context of monocular videos without camera teleportation, as demonstrated in the work [18], DynPoint attains comparable outcomes to previous algorithms. Due to the inherent limitations of having few multi-view perspectives and overlapping information, establishing correspondences between adjacent frames becomes challenging. Consequently, the view synthesis task based on monocular videos proves to be more arduous on this dataset compared to other datasets.

4.2 Ablation Studies

In order to evaluate the effectiveness of the strategies proposed in our paper, we conducted three ablation studies. These studies include: (1) the absence of the multiple-step training strategy outlined in Sec. 3.2 and Sec. 3.3; (2) the utilization of only six frames in the vicinity ($K = 3$); and (3) the exclusion of the hierarchical point cloud. The results are presented in Tab. 5. It is evident from the results that the omission of the multiple-step training strategy leads to the largest drop in performance. Without this strategy, the first stage produces noisy outcomes for both monocular depth and scene flow estimation, consequently hindering the generation of the neural point cloud and impacting the performance of the second stage. Moreover, using a limited number of adjacent frames also adversely affects the final performance, which aligns with our expectations as limited inputs correspond to limited information. Although the removal of the hierarchical point cloud does not significantly degrade performance, it still plays a role in generating finer results.



Figure 6: **Demonstration of Failure Results on Nvidia Dataset.** In this demonstration, we present the failure results generated by DynPoint.

4.3 Consistent Depth & Scene Flow Estimation On Davis

In order to validate the efficacy of the monocular depth estimation technique and the scene flow estimation method, we present the following visualization results: (1) Reconstructed Target Image using Monocular Depth Estimation: We demonstrate the reconstruction of the target image by warping the reference image based on the monocular depth estimation. (2) Reconstructed Target Image using Scene Flow and Depth Estimation: We present the visual reconstruction of the target image achieved through warping the reference image using solely depth estimation or a combination of scene flow estimation and depth estimation. The results are displayed in Fig. 5. Upon observing the second row, it is evident that DynPoint demonstrates commendable performance in reconstructing the static background of the target frame through monocular depth estimation. However, the primary errors (deep red part) occur in the dynamic region, where accounting for object movement becomes crucial for accurate warping. Moving to the third row, our scene flow estimation proves to be effective in capturing the movement of dynamic objects, as in the red error map Fig. 5.

4.4 Failure Cases

Despite the notable achievements of DynPoint, certain failure cases were observed during the view synthesis process, as demonstrated in Fig. 6. By comparing the first and second images, it becomes apparent that generating realistic facial features in regions with intricate details proves to be challenging. Furthermore, when comparing the third and fourth images, it is evident that DynPoint struggles with handling fine objects and reflections, as these aspects heavily rely on the accurate geometry inference obtained in the first stage.

5 Conclusion

In this research paper, we present DynPoint, an algorithm specifically designed to address the view synthesis task for monocular videos. Rather than relying on learning a global representation encompassing color, geometry, and motion information of the entire scene, we propose an approach that aggregates information from neighboring frames. This aggregation process is facilitated by learning correspondences between the target frame and reference frames, aided by depth and scene flow inference. The experimental results demonstrate that our proposed model exhibits improved performance in terms of both accuracy and speed compared to existing approaches.

Acknowledgements. Our research is supported by Amazon Web Services in the Oxford-Singapore Human-Machine Collaboration Programme and by the ACE-OPS project (EP/S030832/1). We are grateful to all of the anonymous reviewers for their valuable comments.

References

- [1] J. T. Barron, B. Mildenhall, M. Tancik, P. Hedman, R. Martin-Brualla, and P. P. Srinivasan, “Mip-nerf: A multiscale representation for anti-aliasing neural radiance fields,” in *Proceedings of the IEEE/CVF International Conference on Computer Vision*, 2021, pp. 5855–5864.
- [2] C. Buehler, M. Bosse, L. McMillan, S. Gortler, and M. Cohen, “Unstructured lumigraph rendering,” in *Proceedings of the 28th annual conference on Computer graphics and interactive techniques*, 2001, pp. 425–432.
- [3] S. Cai, A. Obukhov, D. Dai, and L. Van Gool, “Pix2nerf: Unsupervised conditional p-gan for single image to neural radiance fields translation,” in *Proceedings of the IEEE/CVF Conference on Computer Vision and Pattern Recognition*, 2022, pp. 3981–3990.
- [4] J. Carranza, C. Theobalt, M. A. Magnor, and H.-P. Seidel, “Free-viewpoint video of human actors,” *ACM transactions on graphics (TOG)*, vol. 22, no. 3, pp. 569–577, 2003.
- [5] J.-X. Chai, X. Tong, S.-C. Chan, and H.-Y. Shum, “Plenoptic sampling,” in *Proceedings of the 27th annual conference on Computer graphics and interactive techniques*, 2000, pp. 307–318.
- [6] E. R. Chan, M. Monteiro, P. Kellnhofer, J. Wu, and G. Wetzstein, “pi-gan: Periodic implicit generative adversarial networks for 3d-aware image synthesis,” in *Proceedings of the IEEE/CVF conference on computer vision and pattern recognition*, 2021, pp. 5799–5809.
- [7] G. Chaurasia, S. Duchene, O. Sorkine-Hornung, and G. Drettakis, “Depth synthesis and local warps for plausible image-based navigation,” *ACM Transactions on Graphics (TOG)*, vol. 32, no. 3, pp. 1–12, 2013.
- [8] A. Chen, Z. Xu, F. Zhao, X. Zhang, F. Xiang, J. Yu, and H. Su, “Mvsnerf: Fast generalizable radiance field reconstruction from multi-view stereo,” in *Proceedings of the IEEE/CVF International Conference on Computer Vision*, 2021, pp. 14 124–14 133.
- [9] J. Cheng, C. Wang, and M. Q.-H. Meng, “Robust visual localization in dynamic environments based on sparse motion removal,” *IEEE Transactions on Automation Science and Engineering*, vol. 17, no. 2, pp. 658–669, 2019.
- [10] I. Choi, O. Gallo, A. Troccoli, M. H. Kim, and J. Kautz, “Extreme view synthesis,” in *Proceedings of the IEEE/CVF International Conference on Computer Vision*, 2019, pp. 7781–7790.
- [11] E. De Aguiar, C. Stoll, C. Theobalt, N. Ahmed, H.-P. Seidel, and S. Thrun, “Performance capture from sparse multi-view video,” in *ACM SIGGRAPH 2008 papers*, 2008, pp. 1–10.
- [12] L. Ding and A. Goshtasby, “On the canny edge detector,” *Pattern recognition*, vol. 34, no. 3, pp. 721–725, 2001.
- [13] Y. Du, Y. Zhang, H.-X. Yu, J. B. Tenenbaum, and J. Wu, “Neural radiance flow for 4d view synthesis and video processing,” in *2021 IEEE/CVF International Conference on Computer Vision (ICCV)*. IEEE Computer Society, 2021, pp. 14 304–14 314.
- [14] J. Fang, T. Yi, X. Wang, L. Xie, X. Zhang, W. Liu, M. Nießner, and Q. Tian, “Fast dynamic radiance fields with time-aware neural voxels,” in *SIGGRAPH Asia 2022 Conference Papers*, 2022, pp. 1–9.
- [15] J. Flynn, M. Broxton, P. Debevec, M. DuVall, G. Fyffe, R. Overbeck, N. Snavely, and R. Tucker, “Deepview: View synthesis with learned gradient descent,” in *Proceedings of the IEEE/CVF Conference on Computer Vision and Pattern Recognition*, 2019, pp. 2367–2376.
- [16] J. Flynn, I. Neulander, J. Philbin, and N. Snavely, “Deepstereo: Learning to predict new views from the world’s imagery,” in *Proceedings of the IEEE conference on computer vision and pattern recognition*, 2016, pp. 5515–5524.
- [17] C. Gao, A. Saraf, J. Kopf, and J.-B. Huang, “Dynamic view synthesis from dynamic monocular video,” in *Proceedings of the IEEE/CVF International Conference on Computer Vision*, 2021, pp. 5712–5721.
- [18] H. Gao, R. Li, S. Tulsiani, B. Russell, and A. Kanazawa, “Monocular dynamic view synthesis: A reality check,” in *Advances in Neural Information Processing Systems*, 2022.
- [19] C. Godard, O. Mac Aodha, and G. J. Brostow, “Unsupervised monocular depth estimation with left-right consistency,” in *Proceedings of the IEEE conference on computer vision and pattern recognition*, 2017, pp. 270–279.
- [20] S. J. Gortler, R. Grzeszczuk, R. Szeliski, and M. F. Cohen, “The lumigraph,” in *Proceedings of the 23rd annual conference on Computer graphics and interactive techniques*, 1996, pp. 43–54.
- [21] J. Gu, L. Liu, P. Wang, and C. Theobalt, “Stylenerf: A style-based 3d-aware generator for high-resolution image synthesis,” *arXiv preprint arXiv:2110.08985*, 2021.
- [22] K. Guo, P. Lincoln, P. Davidson, J. Busch, X. Yu, M. Whalen, G. Harvey, S. Orts-Escolano, R. Pandey, J. Dourgarian, *et al.*, “The relightables: Volumetric performance capture of humans with realistic relighting,” *ACM Transactions on Graphics (ToG)*, vol. 38, no. 6, pp. 1–19, 2019.

- [23] R. Hartley and A. Zisserman, *Multiple view geometry in computer vision*. Cambridge university press, 2003.
- [24] K. He, G. Gkioxari, P. Dollár, and R. Girshick, “Mask r-cnn,” in *Proceedings of the IEEE international conference on computer vision*, 2017, pp. 2961–2969.
- [25] P. Hedman, J. Philip, T. Price, J.-M. Frahm, G. Drettakis, and G. Brostow, “Deep blending for free-viewpoint image-based rendering,” *ACM Transactions on Graphics (TOG)*, vol. 37, no. 6, pp. 1–15, 2018.
- [26] Z. Huang, X. Shi, C. Zhang, Q. Wang, K. C. Cheung, H. Qin, J. Dai, and H. Li, “Flowformer: A transformer architecture for optical flow,” in *Computer Vision—ECCV 2022: 17th European Conference, Tel Aviv, Israel, October 23–27, 2022, Proceedings, Part XVII*. Springer, 2022, pp. 668–685.
- [27] N. K. Kalantari, T.-C. Wang, and R. Ramamoorthi, “Learning-based view synthesis for light field cameras,” *ACM Transactions on Graphics (TOG)*, vol. 35, no. 6, pp. 1–10, 2016.
- [28] J. Kopf, F. Langguth, D. Scharstein, R. Szeliski, and M. Goesele, “Image-based rendering in the gradient domain,” *ACM Transactions on Graphics (TOG)*, vol. 32, no. 6, pp. 1–9, 2013.
- [29] M. Levoy and P. Hanrahan, “Light field rendering,” in *Proceedings of the 23rd annual conference on Computer graphics and interactive techniques*, 1996, pp. 31–42.
- [30] Z. Li, S. Niklaus, N. Snavely, and O. Wang, “Neural scene flow fields for space-time view synthesis of dynamic scenes,” in *Proceedings of the IEEE/CVF Conference on Computer Vision and Pattern Recognition*, 2021, pp. 6498–6508.
- [31] Z. Li, Q. Wang, F. Cole, R. Tucker, and N. Snavely, “Dynibar: Neural dynamic image-based rendering,” *arXiv preprint arXiv:2211.11082*, 2022.
- [32] K.-E. Lin, L. Xiao, F. Liu, G. Yang, and R. Ramamoorthi, “Deep 3d mask volume for view synthesis of dynamic scenes,” in *Proceedings of the IEEE/CVF International Conference on Computer Vision*, 2021, pp. 1749–1758.
- [33] L. Liu, J. Gu, K. Zaw Lin, T.-S. Chua, and C. Theobalt, “Neural sparse voxel fields,” *Advances in Neural Information Processing Systems*, vol. 33, pp. 15 651–15 663, 2020.
- [34] Y.-L. Liu, C. Gao, A. Meuleman, H.-Y. Tseng, A. Saraf, C. Kim, Y.-Y. Chuang, J. Kopf, and J.-B. Huang, “Robust dynamic radiance fields,” *arXiv preprint arXiv:2301.02239*, 2023.
- [35] S. Lombardi, T. Simon, J. Saragih, G. Schwartz, A. Lehrmann, and Y. Sheikh, “Neural volumes: Learning dynamic renderable volumes from images,” *ACM Trans. Graph.*, vol. 38, no. 4, pp. 65:1–65:14, July 2019.
- [36] B. Mildenhall, P. P. Srinivasan, M. Tancik, J. T. Barron, R. Ramamoorthi, and R. Ng, “Nerf: Representing scenes as neural radiance fields for view synthesis,” in *European conference on computer vision*. Springer, 2020, pp. 405–421.
- [37] ———, “Nerf: Representing scenes as neural radiance fields for view synthesis,” *Communications of the ACM*, vol. 65, no. 1, pp. 99–106, 2021.
- [38] M. Niemeyer, J. T. Barron, B. Mildenhall, M. S. Sajjadi, A. Geiger, and N. Radwan, “Regnerf: Regularizing neural radiance fields for view synthesis from sparse inputs,” in *Proceedings of the IEEE/CVF Conference on Computer Vision and Pattern Recognition*, 2022, pp. 5480–5490.
- [39] M. Niemeyer and A. Geiger, “Giraffe: Representing scenes as compositional generative neural feature fields,” in *Proceedings of the IEEE/CVF Conference on Computer Vision and Pattern Recognition*, 2021, pp. 11 453–11 464.
- [40] M. Niemeyer, L. Mescheder, M. Oechsle, and A. Geiger, “Differentiable volumetric rendering: Learning implicit 3d representations without 3d supervision,” in *Proceedings of the IEEE/CVF Conference on Computer Vision and Pattern Recognition*, 2020, pp. 3504–3515.
- [41] K. Park, U. Sinha, J. T. Barron, S. Bouaziz, D. B. Goldman, S. M. Seitz, and R. Martin-Brualla, “Nerfies: Deformable neural radiance fields,” in *Proceedings of the IEEE/CVF International Conference on Computer Vision*, 2021, pp. 5865–5874.
- [42] K. Park, U. Sinha, P. Hedman, J. T. Barron, S. Bouaziz, D. B. Goldman, R. Martin-Brualla, and S. M. Seitz, “Hypernerf: A higher-dimensional representation for topologically varying neural radiance fields,” *arXiv preprint arXiv:2106.13228*, 2021.
- [43] Y. Peng, Y. Yan, S. Liu, Y. Cheng, S. Guan, B. Pan, G. Zhai, and X. Yang, “Cagenerf: Cage-based neural radiance field for generalized 3d deformation and animation,” *Advances in Neural Information Processing Systems*, vol. 35, pp. 31 402–31 415, 2022.
- [44] F. Perazzi, J. Pont-Tuset, B. McWilliams, L. Van Gool, M. Gross, and A. Sorkine-Hornung, “A benchmark dataset and evaluation methodology for video object segmentation,” in *Proceedings of the IEEE conference on computer vision and pattern recognition*, 2016, pp. 724–732.

- [45] A. Pumarola, E. Corona, G. Pons-Moll, and F. Moreno-Noguer, “D-nerf: Neural radiance fields for dynamic scenes,” in *Proceedings of the IEEE/CVF Conference on Computer Vision and Pattern Recognition*, 2021, pp. 10 318–10 327.
- [46] R. Ranftl, A. Bochkovskiy, and V. Koltun, “Vision transformers for dense prediction,” in *Proceedings of the IEEE/CVF International Conference on Computer Vision*, 2021, pp. 12 179–12 188.
- [47] R. Ranftl, K. Lasinger, D. Hafner, K. Schindler, and V. Koltun, “Towards robust monocular depth estimation: Mixing datasets for zero-shot cross-dataset transfer,” *IEEE transactions on pattern analysis and machine intelligence*, vol. 44, no. 3, pp. 1623–1637, 2020.
- [48] G. Riegler and V. Koltun, “Free view synthesis,” in *Computer Vision–ECCV 2020: 16th European Conference, Glasgow, UK, August 23–28, 2020, Proceedings, Part XIX 16*. Springer, 2020, pp. 623–640.
- [49] J. L. Schonberger and J.-M. Frahm, “Structure-from-motion revisited,” in *Proceedings of the IEEE conference on computer vision and pattern recognition*, 2016, pp. 4104–4113.
- [50] K. Schwarz, Y. Liao, M. Niemeyer, and A. Geiger, “Graf: Generative radiance fields for 3d-aware image synthesis,” *Advances in Neural Information Processing Systems*, vol. 33, pp. 20 154–20 166, 2020.
- [51] V. Sitzmann, J. Martel, A. Bergman, D. Lindell, and G. Wetzstein, “Implicit neural representations with periodic activation functions,” *Advances in Neural Information Processing Systems*, vol. 33, pp. 7462–7473, 2020.
- [52] V. Sitzmann, J. Thies, F. Heide, M. Nießner, G. Wetzstein, and M. Zollhofer, “Deepvoxels: Learning persistent 3d feature embeddings,” in *Proceedings of the IEEE/CVF Conference on Computer Vision and Pattern Recognition*, 2019, pp. 2437–2446.
- [53] V. Sitzmann, M. Zollhöfer, and G. Wetzstein, “Scene representation networks: Continuous 3d-structure-aware neural scene representations,” *Advances in Neural Information Processing Systems*, vol. 32, 2019.
- [54] P. P. Srinivasan, R. Tucker, J. T. Barron, R. Ramamoorthi, R. Ng, and N. Snavely, “Pushing the boundaries of view extrapolation with multiplane images,” in *Proceedings of the IEEE/CVF Conference on Computer Vision and Pattern Recognition*, 2019, pp. 175–184.
- [55] Z. Teed and J. Deng, “Raft: Recurrent all-pairs field transforms for optical flow,” in *Computer Vision–ECCV 2020: 16th European Conference, Glasgow, UK, August 23–28, 2020, Proceedings, Part II 16*. Springer, 2020, pp. 402–419.
- [56] E. Tretschk, A. Tewari, V. Golyanik, M. Zollhöfer, C. Lassner, and C. Theobalt, “Non-rigid neural radiance fields: Reconstruction and novel view synthesis of a dynamic scene from monocular video,” in *Proceedings of the IEEE/CVF International Conference on Computer Vision*, 2021, pp. 12 959–12 970.
- [57] A. Trevisan and B. Yang, “Grf: Learning a general radiance field for 3d representation and rendering,” in *Proceedings of the IEEE/CVF International Conference on Computer Vision*, 2021, pp. 15 182–15 192.
- [58] C. Wang, B. Eckart, S. Lucey, and O. Gallo, “Neural trajectory fields for dynamic novel view synthesis,” *arXiv preprint arXiv:2105.05994*, 2021.
- [59] Q. Wang, Z. Wang, K. Genova, P. P. Srinivasan, H. Zhou, J. T. Barron, R. Martin-Brualla, N. Snavely, and T. Funkhouser, “Ibrnet: Learning multi-view image-based rendering,” in *Proceedings of the IEEE/CVF Conference on Computer Vision and Pattern Recognition*, 2021, pp. 4690–4699.
- [60] S. Wizadwongsa, P. Phongthawee, J. Yenphraphai, and S. Suwajanakorn, “Nex: Real-time view synthesis with neural basis expansion,” in *Proceedings of the IEEE/CVF Conference on Computer Vision and Pattern Recognition*, 2021, pp. 8534–8543.
- [61] H. Xu, T. Alldieck, and C. Sminchisescu, “H-nerf: Neural radiance fields for rendering and temporal reconstruction of humans in motion,” *Advances in Neural Information Processing Systems*, vol. 34, pp. 14 955–14 966, 2021.
- [62] Q. Xu, Z. Xu, J. Philip, S. Bi, Z. Shu, K. Sunkavalli, and U. Neumann, “Point-nerf: Point-based neural radiance fields,” in *Proceedings of the IEEE/CVF Conference on Computer Vision and Pattern Recognition*, 2022, pp. 5438–5448.
- [63] G. Yang, M. Vo, N. Neverova, D. Ramanan, A. Vedaldi, and H. Joo, “Banmo: Building animatable 3d neural models from many casual videos,” in *Proceedings of the IEEE/CVF Conference on Computer Vision and Pattern Recognition*, 2022, pp. 2863–2873.
- [64] G. Yang, C. Wang, N. D. Reddy, and D. Ramanan, “Reconstructing animatable categories from videos,” *arXiv preprint arXiv:2305.06351*, 2023.
- [65] J. S. Yoon, K. Kim, O. Gallo, H. S. Park, and J. Kautz, “Novel view synthesis of dynamic scenes with globally coherent depths from a monocular camera,” in *Proceedings of the IEEE/CVF Conference on Computer Vision and Pattern Recognition*, 2020, pp. 5336–5345.
- [66] A. Yu, V. Ye, M. Tancik, and A. Kanazawa, “pixelnerf: Neural radiance fields from one or few images,” in *Proceedings of the IEEE/CVF Conference on Computer Vision and Pattern Recognition*, 2021, pp. 4578–4587.

- [67] K. Zhang, G. Riegler, N. Snavely, and V. Koltun, “Nerf++: Analyzing and improving neural radiance fields,” *arXiv preprint arXiv:2010.07492*, 2020.
- [68] Z. Zhang, F. Cole, Z. Li, M. Rubinstein, N. Snavely, and W. T. Freeman, “Structure and motion from casual videos,” in *Computer Vision—ECCV 2022: 17th European Conference, Tel Aviv, Israel, October 23–27, 2022, Proceedings, Part XXXIII*. Springer, 2022, pp. 20–37.
- [69] K. Zhou, J. Bian, Q. Xie, J. Zheng, N. Trigoni, and A. Markham, “Manydepth2: Motion-aware self-supervised monocular depth estimation in dynamic scenes,” *arXiv preprint arXiv:2312.15268*, 2023.
- [70] K. Zhou, C. Chen, B. Wang, M. R. U. Saputra, N. Trigoni, and A. Markham, “Vmloc: Variational fusion for learning-based multimodal camera localization,” in *Proceedings of the AAAI Conference on Artificial Intelligence*, vol. 35, no. 7, 2021, pp. 6165–6173.
- [71] K. Zhou, L. Hong, C. Chen, H. Xu, C. Ye, Q. Hu, and Z. Li, “Devnet: Self-supervised monocular depth learning via density volume construction,” in *Computer Vision—ECCV 2022: 17th European Conference, Tel Aviv, Israel, October 23–27, 2022, Proceedings, Part XXXIX*. Springer, 2022, pp. 125–142.
- [72] K. Zhou, L. Hong, E. Xie, Y. Yang, Z. Li, and W. Zhang, “Serf: Fine-grained interactive 3d segmentation and editing with radiance fields,” *arXiv preprint arXiv:2312.15856*, 2023.
- [73] T. Zhou, R. Tucker, J. Flynn, G. Fyffe, and N. Snavely, “Stereo magnification: Learning view synthesis using multiplane images,” *arXiv preprint arXiv:1805.09817*, 2018.

6 Appendix

6.1 Network Structure

In this section, we present the architectural details of the scene flow MLP and rendering MLP models to facilitate the reproducibility of our experiments. These architectures serve as crucial components in our framework and play a significant role in the overall scene flow estimation and rendering processes. By providing the detailed specifications of these models, we aim to enable researchers and practitioners to reproduce our results effectively and potentially build upon our work for further advancements in the field.

Scene Flow MLP: To expedite the inference process, we have devised a formulation for the MLP utilizing a Convolutional Network Structure with the kernel size (1×1) . This architectural design choice allows for enhanced computational efficiency and speed during the inference phase. Rather than processing position information (x, y, z) on a point-by-point basis, we adopt a holistic approach by considering the entire image’s points as input. These points are concatenated with additional embedded information, including the positional information $e(x, y, z)$, the temporal information t , and the embedded temporal information $e(t)$. This comprehensive input configuration allows for a more comprehensive understanding of the scene, incorporating both spatial and temporal cues. By incorporating these additional embeddings, our model gains a richer representation of the data, enabling it to capture intricate relationships and dependencies between points in the image, thereby enhancing its ability to make accurate predictions. The structure of scene flow MLP is shown in the upper part of Fig. 7.

Rendering MLP: The rendering MLP, depicted in Fig. 8, takes position q and direction d as inputs to predict density σ and color c . It employs M points \hat{P}_t^m around radius R of the queried point q , with point-wise feature \mathcal{F}^m , processed by a feature network. The feature network outputs point-wise features $\hat{\mathcal{F}}_t^m$, used to compute a weighted summation $\bar{\mathcal{F}}_t$ with weights (the product of the inverse distance between \hat{P}_t^m & q and the confidence score γ_t^m , which is demonstrated by **arrow**). This summation is concatenated with direction d and passed through a Color network to compute final color c . Simultaneously, $\hat{\mathcal{F}}_t^m$ is used in the Density network to predict point-wise density σ_t^m , which is weightedly summed to obtain the final density σ . Eqn. 9 utilizes both density σ and color c to compute pixel-wise color information C . The Feature Net, Density Net, and Color Net consist of three fully connected layers.

7 Pose Correction For Colmap

Pose estimation in dynamic scenarios is consistently a challenging endeavor [70, 9]. Our investigation reveals that in scenarios where the precise ground truth pose is not available, and the estimation of transformation pose is dependent on the original COLMAP, there is a possibility of obtaining inaccurate pose estimations. This, in turn, can have a detrimental impact on the effectiveness of our depth and scene flow estimation processes. The optimization of scale parameters, denoted as α_t & β_t , relies on the triangulated depth estimation, denoted as \bar{D}_t . However, it is important to note that the accuracy of \bar{D}_t is influenced by the accuracy of the camera configuration, represented by the matrix $[\mathbf{R}_{t,c}, \mathbf{t}_{t,c}]$. Despite the incorporation of a motion mask in the COLMAP framework, accurate pose estimation is still a challenge in scenarios characterized by either texture-less environments or small camera motions. These conditions hinder the ability of COLMAP to effectively estimate precise pose information. To enhance the accuracy of pose estimation, we combine COLMAP with previously estimated mask, represented as \mathcal{M}_f .

7.1 Experimental Details

7.1.1 Evaluation Metrics

PSNR and mPSNR: Peak signal-to-noise ratio (PSNR) and mean peak signal-to-noise ratio (mPSNR) are widely used evaluation metrics in image and video processing to assess the quality of a processed or reconstructed signal relative to a reference signal. Expressed in decibels (dB), PSNR is calculated by comparing the Mean Squared Error (MSE) between the original and processed signals. The

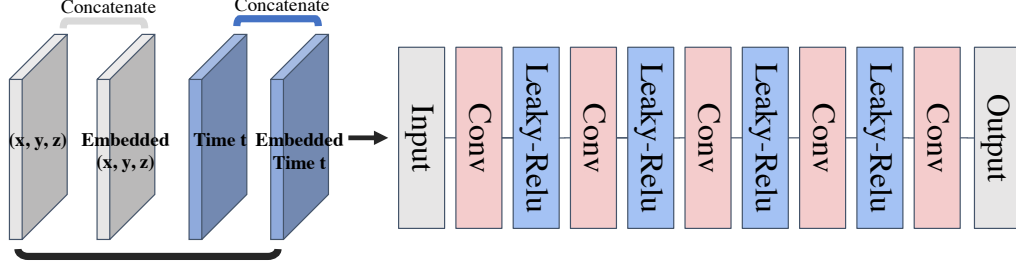


Figure 7: **Structure of Network.** The scene flow network architecture, depicted in the figure, is utilized in the initial stage of our pipeline. It takes 3D position (x, y, z) and time information t as input and predicts both forward and backward scene flow.

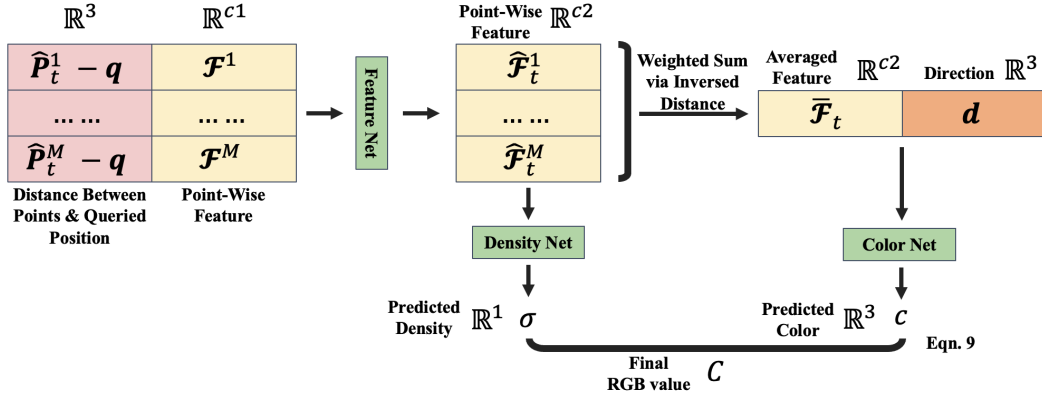


Figure 8: **Structure of Network.** The rendering network architecture, illustrated in the figure, is employed in the second stage of our pipeline. It takes queried points q and direction d as input and predicts the final pixel-wise color C .

formula for PSNR is as follows:

$$PSNR = 10 * \log_{10}((MAX^2)/MSE) \quad (10)$$

Here, MAX represents the maximum possible pixel value of the signal (typically 255 for an 8-bit image), and MSE is the mean squared difference between the original and processed signals.

A higher PSNR value indicates lower levels of distortion or error, indicating better fidelity to the original signal. In essence, a higher PSNR value signifies a higher degree of similarity between the original and processed signals.

LPIPS: LPIPS (Learned Perceptual Image Patch Similarity) is a metric used to measure the similarity between images based on perceptual features. It leverages a deep neural network to map image patches to perceptual similarity scores. The process involves preprocessing the images, extracting features using a pre-trained neural network, extracting image patches, computing similarity between corresponding patches, aggregating patch similarity scores, and normalizing the similarity score. LPIPS has demonstrated strong correlation with human perception and finds applications in image quality assessment and image-to-image translation. Its utilization allows researchers and practitioners to evaluate the performance and quality of computer vision algorithms by quantifying perceptual similarity between images.

mSSIM: Mean Structural Similarity Index (mSSIM) is an objective image quality metric that measures the similarity between a reference image and a distorted image. It extends the Structural Similarity Index (SSIM) by considering multiple scales of image details. It divides the images into scales, calculates the SSIM index for each scale using luminance, contrast, and structure information, and averages the weighted SSIM index values to obtain the mSSIM value (-1 to 1). Higher mSSIM values indicate better image quality. However, mSSIM may not always align perfectly with human perception, so it is often used in conjunction with other metrics and subjective testing for a more comprehensive assessment.

7.1.2 Datasets

Nvidia Dataset: Our method is evaluated on the Dynamic Scene Dataset [65], which comprises 9 video sequences. The sequences are captured using a static camera rig consisting of 12 cameras. Simultaneous images are captured by all 12 cameras at 12 different time steps $\{t_0, t_1, \dots, t_{11}\}$. The input consists of monocular videos with twelve frames, denoted as $\{I_0, I_1, \dots, I_{11}\}$, where each frame is obtained by sampling an image from the i -th camera at time t_i . Notably, each frame of the video is captured using a different camera to simulate camera motion. The frames contain a background that remains static over time, as well as a dynamic object that exhibits temporal variations. To estimate camera poses and the near and far bounds of the scene, we employ COLMAP, following a similar approach to NeRF [36]. We assume a shared intrinsic parameter for all cameras. Following [17, 34], we use Jumping, Skating, Truck, Umbrella, Balloon1, Balloon2 and Playground, 7 scenes for our evaluation. Lastly, we resize all sequences to a resolution of 480×270 .

Nerfie Dataset: Our method was evaluated on the Nerfie [41]. The dataset employs two methods for data capture: (a) capturing synchronized selfies using the front-facing camera, achieving sub-millisecond synchronization, and (b) recording two videos with the back-facing camera, manually synchronizing them based on audio, and subsampling to 5 frames per second. Image registration was performed using COLMAP [49] with rigid relative camera pose constraints. Sequences captured with method (a) have fewer frames (40-78), but precise synchronization of focus, exposure, and timing. Sequences captured with method (b) have denser temporal sampling (193-356 frames), but less precise synchronization with potential variations in exposure and focus between the cameras. Following the dataset’s configuration, we divided the dataset into training and testing sets. The left view was assigned to the training set and the right view to the validation set, and vice versa, in an alternating manner. This allocation ensures that all areas of the scene have been observed by at least one camera, preventing unobserved regions.

Iphone Dataset: In this study, we extend the evaluation of our proposed method by applying it to the more challenging Iphone dataset introduced by [18]. This dataset comprises 14 sequences that exhibit non-repetitive motion, encompassing diverse categories such as generic objects, humans, and pets. To conduct our evaluation, we follow the setup in [18] consisting of three cameras for multi-camera capture. Specifically, one camera is handheld and in motion during the training phase, while the other two cameras remain static with a large baseline and are used for evaluation purposes. Additionally, the Iphone dataset provides metric depth information obtained from lidar sensors, which can be utilized for supervising the depth estimation task.

Davis Dataset: To test the performance of monocular depth estimation and scene flow estimation module, we also provide the visualization result on the DAVIS (Densely Annotated Video Segmentation) dataset [44], which is a benchmark dataset commonly used in computer vision research for the task of video object segmentation.

7.2 Depth Visualization

In this section, we present the visual point cloud results obtained from the consistent depth estimation module applied to the Nvidia dataset [65]. In our methodology, we incorporate a pose refinement algorithm to enhance the accuracy of pose estimation, which is initially obtained using COLMAP. By utilizing this pose refinement algorithm, we aim to improve the quality of the depth estimation process. The visualization of the point cloud results allows for a comprehensive evaluation of the effectiveness of our proposed approach in achieving accurate and consistent depth estimation on the Nvidia dataset shown in Fig. 9. It is apparent that estimating depth generally allows us to perceive the shape and size of objects in various situations.

8 Scene Flow Visualization

This section presents additional visualization results of error maps obtained from the Davis dataset. These results serve to demonstrate the performance of our proposed scene flow module in handling two specific scenarios: (1) the presence of fine details, represented by the train scenario, and (2) the occurrence of motion blur, exemplified by the dog scenario. These visualizations provide a comprehensive understanding of how our method performs in challenging situations where fine details and motion blur are prevalent shown in Fig. 10.



Figure 9: **Point Cloud Based on Depth Estimation.** This figure presents the accuracy of estimated depth, with the upper portion depicting the original images and the lower portion representing the point cloud generated using depth information and camera matrix.

8.1 Difference with NSFF

The NSFF paper has undeniably made a significant contribution to the realm of monocular view synthesis by integrating scene flow into the framework of monocular video-based algorithms. However, there are several differences that set NSFF and DynPoint apart. Firstly, DynPoint introduces a corrective mechanism to adjust the depth scale obtained from monocular videos. This correction greatly improves the consistency of geometry across different frames. Furthermore, NSFF predicts flow for all points (128) along a ray, while DynPoint focuses exclusively on predicting scene flow for surface points. This approach brings two important advantages: firstly, it adds specific constraints to the scene flow of surface points by using predicted optic flow and depth information, which significantly enhances the learning process; secondly, by concentrating on surface points, the scene flow prediction process is made faster. Lastly, unlike NSFF, which encodes information extensively within the MLP, DynPoint gathers information from neighboring frames using 3D correspondence. This unique approach empowers DynPoint to more effectively learn from sequences of long videos.

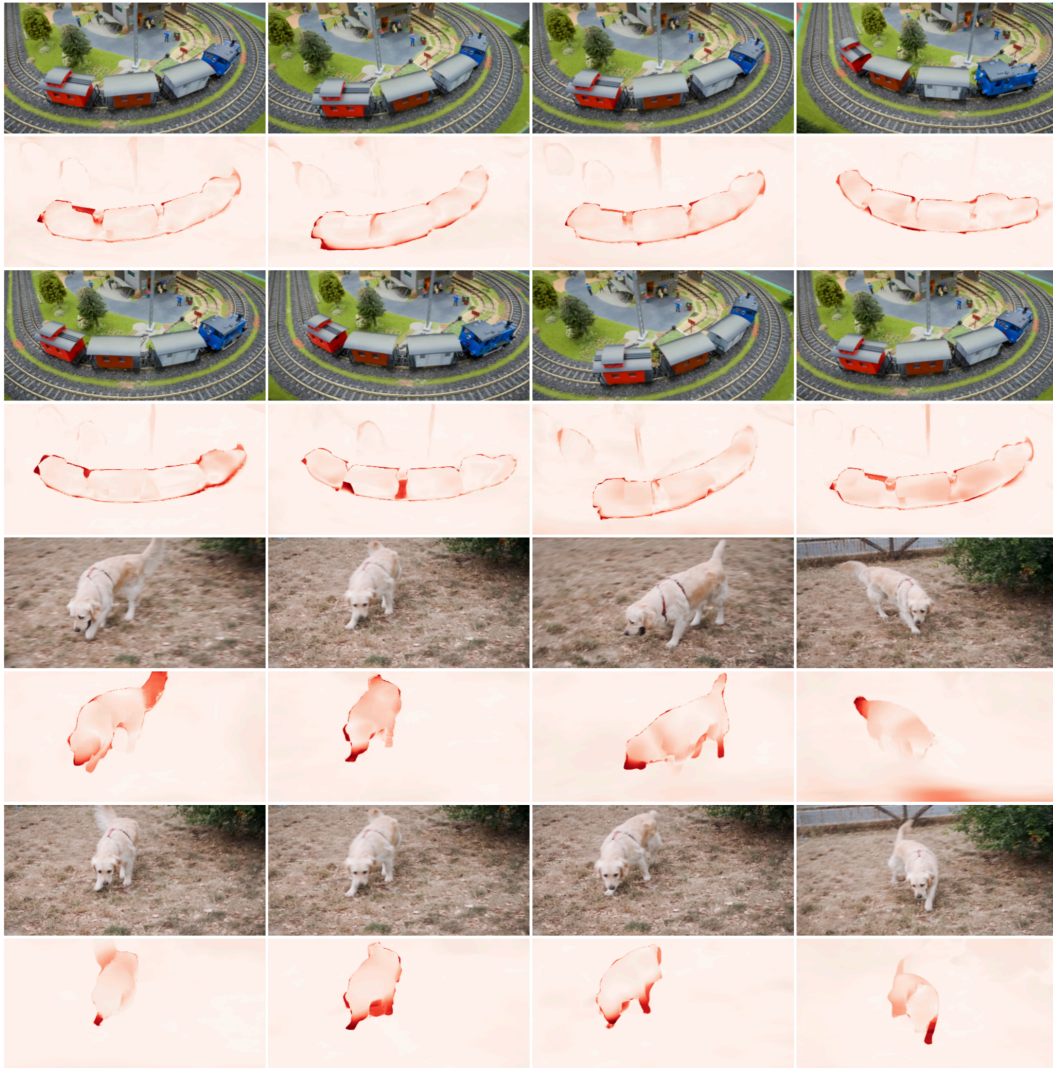


Figure 10: **Demonstration of Scene Flow Estimation.** The odd rows (1, 3, 5, 7) of the presented data exhibit the original images, while the even rows (2, 4, 6, 8) display the error map. Error map represented by the intensity of red is provided to visualize the performance, where deeper shades of red indicate larger errors (in terms of pixel movement based on scene flow compared to optic flow).